

# Magnetized and collimated millimeter scale plasma jets with astrophysical relevance

Parrish C. Brady,<sup>1</sup> Hernan J. Quevedo,<sup>1</sup> Prashant M. Valanju,<sup>2</sup> Roger D. Bengtson,<sup>3</sup> and Todd Ditmire<sup>3</sup>

<sup>1</sup>Texas Center for High Intensity Laser Science, University of Texas at Austin, Austin, Texas 78712, USA

<sup>2</sup>Institute for Fusion Studies, University of Texas at Austin, Austin, Texas 78712-1060, USA

<sup>3</sup>Department of Physics, University of Texas at Austin, Austin, Texas 78712, USA

(Received 21 July 2011; accepted 2 November 2011; published online 31 January 2012)

Magnetized collimated plasma jets are created in the laboratory to extend our understanding of plasma jet acceleration and collimation mechanisms with particular connection to astrophysical jets. In this study, plasma collimated jets are formed from supersonic unmagnetized flows, mimicking a stellar wind, subject to currents and magnetohydrodynamic forces. It is found that an external poloidal magnetic field, like the ones found anchored to accretion disks, is essential to stabilize the jets against current-driven instabilities. The maximum jet length before instabilities develop is proportional to the field strength and the length threshold agrees well with Kruskal-Shafranov theory. The plasma evolution is modeled qualitatively using MHD theory of current-carrying flux tubes showing that jet acceleration and collimation arise as a result of electromagnetic forces. © 2012 American Institute of Physics. [doi:10.1063/1.3671953]

## I. INTRODUCTION

Astrophysical jets are self-organized plasmas that can reach velocities near the speed of light and remain collimated up to thousands of light years.<sup>1,2</sup> These jets emanate from very different astrophysical objects such as young stellar objects (YSOs), white dwarfs, active galactic nuclei (AGN), x-ray binaries, among others.<sup>1</sup> The jets from YSOs, for example, present great structure in their morphology, creating Herbig-Haro (HH) objects like HH-34 and HH-47. Jets seem to play an important role in early stellar evolution<sup>3</sup> and are even associated with gamma ray bursts<sup>4</sup> so there has been a considerable amount of research focused in understanding the process of jet formation and collimation. The two proposed mechanisms are magnetohydrodynamically (MHD) or purely hydrodynamically driven, which are based on the role that magnetic fields and radiation cooling play, respectively.<sup>5</sup> Magnetic fields are assumed to have some role in the collimation and flow velocities of the jets<sup>6</sup> although the specifics of their function are still in question. Other features in jets such as knotting have been postulated to be magnetically produced through instabilities.<sup>3</sup> Recently, the Very Long Baseline Array (VLBA) telescope<sup>7</sup> revealed that self organization into a collimated relativistic jet from the active galactic nuclei of M87 occurs thousands light years away from the jet's origin rendering the collimation mechanism enigmatic. Computer simulations propose that jets can be MHD driven close to the origin and purely hydrodynamically driven far away where the field is small.<sup>8</sup>

The morphological similarities present in astrophysical jets with vastly different scale lengths and parameters suggest that there should be some basic principles that apply to all of them in the formation and collimation process. Ryutov<sup>9</sup> showed that two systems described by the ideal MHD equa-

tions will evolve similarly when the Euler number  $Eu = v\sqrt{\rho/p}$  (where  $v$ ,  $\rho$ , and  $p$  are the plasma velocity, density, and pressure, respectively) and the plasma beta  $\beta = p/(B^2/2\mu_0)$  (where  $B$  is the magnetic field) are the same in both systems, and if the initial conditions are geometrically similar. This work opened the possibility to simulate astrophysical phenomena quantitatively in the laboratory and to compare laboratory simulations to astrophysical theory, numerical modeling results and observations. The similarity transformation requires ideal MHD (particles are localized and dissipative processes as well as radiative cooling are small), and the gas to be polytropic, that is, the internal energy proportional to the pressure. The astrophysical length, mass density, and pressure can be scaled by multiplying the same quantities in the lab with factors  $a$ ,  $b$ , and  $c$ , respectively. Simultaneously, the magnetic field, velocity, and time are scaled as  $\sqrt{c}$ ,  $\sqrt{c/b}$ , and  $a\sqrt{b/c}$ , respectively. The mass density for example would be  $\rho_{lab}(r,t) = (1/b) \cdot \rho_{astro}(a \cdot r, a\sqrt{b/c} \cdot t)$ .

Laboratory experiments have produced jets for the purpose of understanding the process of launching and collimation of astrophysical jets.<sup>5</sup> Farley *et al.*<sup>10</sup> and Lebedev *et al.*<sup>11</sup> among others created jets following the hydrodynamically driven approach by coalescing ablated material to form a jet on axis and studying the collimation produced by radiative cooling. Experiments that address the role of magnetic fields have been conducted among others by Lebedev *et al.*<sup>12,13</sup> Hsu *et al.*<sup>14-17</sup> and You *et al.*<sup>18</sup> with very different plasma parameters and geometries. Lebedev *et al.*<sup>12</sup> used a radial wire array z-pinch to create magnetic towers with current driven toroidal magnetic fields. It was found that fields can create outflows and collimation can be the result of radiative cooling. Suzuki-Vidal and Lebedev *et al.*<sup>19</sup> were also able to produce episodes of tower eruptions using foils instead of wires.

Hsu *et al.*<sup>14</sup> in contrast used a coaxial gun with a combination of external poloidal magnetic field and plasma current driven toroidal fields. They found that MHD forces from the flared plasma current profile given by the imposed poloidal field can accelerate the jets. The collimation arises as a result of the magnetic field piling up as it is being carried by the plasma while increasing the pinch effect. The different experiments show that there is no established solution for the process of launching and collimation of jets. Our experiment is aimed at understanding the role of magnetic fields as the proposed collimation mechanism. We find that an external poloidal field is required to stabilize the jets and that acceleration and collimation arise as a result of electromagnetic forces. The maximum jet length before instabilities develop is proportional to the magnetic field strength and the length threshold agrees well with Kruskal-Shafranov theory.

The concept design to create magnetically collimated plasma jets with boundary conditions similar to astrophysical jets is shown in Figure 1. Here, we try to reproduce the origin of the jets and the possible collimation mechanism. An axially symmetric electrode configuration similar to a plasma gun creates a radial electric field ( $E$ ) embedded in a poloidal external magnetic field ( $B_{ext}$ ). Plasma created under this field combination is set into sheared toroidal rotation with velocity  $V_E = E/B_{ext}$ . The set up resembles a rotating stellar accretion disk threaded by the stars' poloidal magnetic field.<sup>14</sup> An uncollimated supersonic molybdenum flow is ejected from the vicinity of the center electrode with similar opening angle as a thermally driven wind from the star system.<sup>20,21</sup> For YSO jets, reported plasma parameters are on the order of  $l \sim 1 \times 10^{14}$  m,  $n \sim 1 \times 10^9$  m<sup>-3</sup>,  $\rho \sim 2 \times 10^{-18}$  Kg/m<sup>3</sup>,  $p \sim 1.6 \times 10^{-10}$  Pa,  $t \sim 1 \times 10^9$  s,  $B \sim 2$  mT,  $v \sim 1 \times 10^5$  m/s, and  $T \sim 1$  eV.<sup>22,23</sup> These parameters give an Euler number of approximately 10 and a  $\beta$  on the order of 1 for the YSO jet system. The general parameters from our experiments are  $l \sim 0.01$  m,  $n = 8 \pm 4 \times 10^{22}$  m<sup>-3</sup>,  $\rho = 0.013 \pm 0.0063$  Kg/m<sup>3</sup>,  $p \sim 1 \times 10^5$  Pa,  $t \sim 2.0 \times 10^{-7}$  s,  $B = 0.4 \pm 0.1$  T,  $v = 4.4 \pm 0.9 \times 10^4$  m/s, and  $T = 6 \pm 3$  eV. The experiment has similar Euler number and  $\beta$  ( $Eu = 18 \pm 9$  and  $\beta = 1.2 \pm 1$ ) as the YSO jets and the values for the scaling factors introduced earlier are  $a \sim 10^{16}$ ,  $b \sim 10^{-16}$ , and  $c \sim 10^{-15}$ . The experimental parameters have been chosen in order to test the scaling theory and universality of these entities. The Reynolds number is

$\sim 10^3 \gg 1$  making viscosity negligible as required by the scaling theory. The magnetic Reynolds number as well as the Peclet number are  $\sim 5$  to 10 which will produce some magnetic diffusion and energy transport by thermal conduction instead of advection. This pushes the parameters of this experiment slightly out of the of scalability requirements which will render the scaling significance in the experiment more qualitative.

## II. EXPERIMENTAL SETUP

The layout of our experimental set up is shown in Figure 2. The millimeter scale plasma gun electrode consists of a grounded thin molybdenum plate with a 10 mm diameter hole and a biased 0.5 mm diameter molybdenum wire in the center of the hole. The wire is aligned perpendicular to the grounded plate and the tip is coplanar with the plate. The electrodes are connected directly, without a switch, to a 5 kV, 2.4  $\mu$ F capacitor. The plasma gun is located inside a vacuum chamber made of an 8 in. diameter stainless steel 6-way-cross at a pressure of 1 mTorr. The pressure-distance product between the electrodes is such that the applied voltage is smaller than the breakdown voltage threshold given by the Paschen curve.<sup>24</sup> An aluminum wire is placed near the plasma gun using a xyz manipulator and a 200 mJ, 1064 nm, and 8 ns pulse duration YAG laser beam focuses on the wire generating a plasma. The location of the aluminum wire is not critical. This laser-produced plasma lowers the breakdown voltage threshold below the applied voltage triggering a discharge between the electrode gap that is followed by a ringing capacitor discharge. The laser triggering mechanism provides high shot to shot reproducibility. The bottom half of the central electrode is surrounded by a small cavity with a flared nozzle at its opening. The center electrode heats up and boils off when the discharge takes place creating a high pressure molybdenum plasma with a low degree of ionization inside the cavity that flows through the nozzle creating an uncollimated supersonic jet. We use this jet as the initial condition of the collimation mechanism and note that this has similarity to a stellar wind from which an astrophysical jet can form. The electrode configuration is placed in various positions and angles in the presence of a magnetic field ( $B_{ext,max} \sim 0.5$  T) to study its role in jet formation, collimation, and stability. The main diagnostics consist of a Princeton Instruments intensified charged-coupled device (ICCD) to capture plasma emission from the electrode discharge. The camera takes single frames with an exposure time of 4.0 ns. High shot to shot reproducibility allows combining frames taken at different time delays and from different shots with same initial conditions to reconstruct the plasma evolution. Filters BG-39 and BG-18 are used to block scattered light from the YAG beam protecting the camera. A Wollaston interferometer<sup>25</sup> was built to measure the density of the ablated molybdenum plasma where possible. The interferometer uses a 532 nm YAG laser beam with 2 ns pulse duration and the plasma interaction with the interference pattern was imaged on a CCD camera. The oscillating current of the discharge is measured using a Rogowski coil while the voltage is measured using a high voltage probe connected at the capacitor leads.

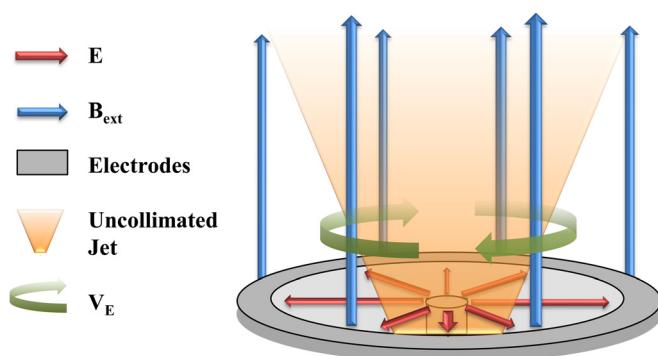


FIG. 1. (Color online) Concept design for the formation of magnetically collimated plasma jets.

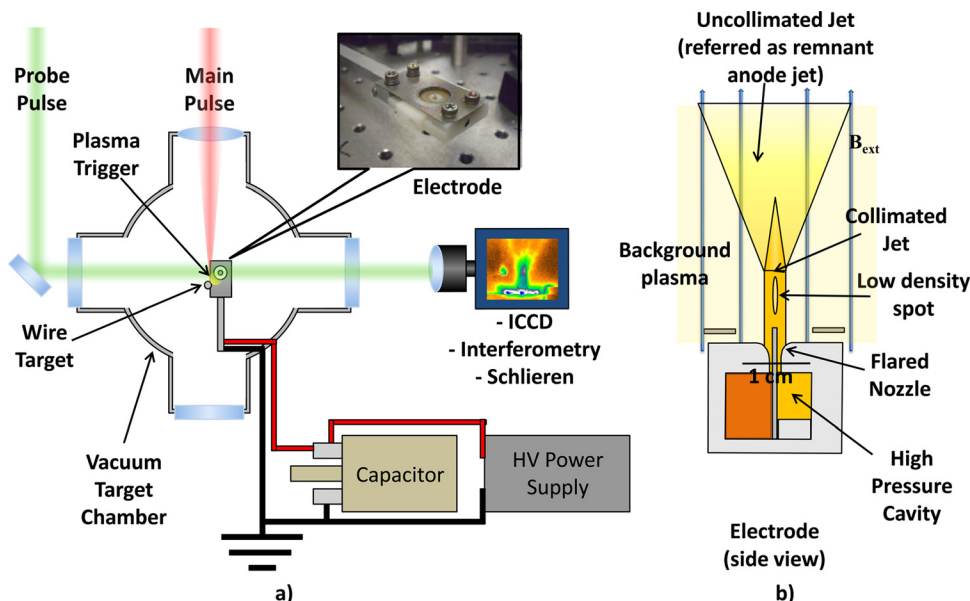


FIG. 2. (Color online) The experimental set up consists of a millimeter scale plasma gun electrode located inside a vacuum chamber connected directly to a capacitor. The main laser beam focuses on an aluminum wire to trigger the current flow. The bottom half of the central electrode is surrounded by a small cavity with a flared nozzle at its opening generating supersonic flows. An ICCD camera is used to capture plasma emission from the discharge while an interferometer measured the density of the ablated plasma.

### III. EXPERIMENTAL RESULTS AND DISCUSSION

The evolution of the discharge after the laser triggers the plasma gun depends on the initial bias polarity as a result of the asymmetry between cathode and anode modes in electrode ablation. In vacuum electrode ablations, the anode heats up globally, while the cathode forms small non-stationary spots of intense temperatures greater than the anode ablation.<sup>24,26</sup> We found that only an initial positive voltage applied to the center conductor allows access to collimated plasma jets in the second half cycle of the discharge. With the center electrode initially positive biased, current flows out of the electrode while heating it up (Figure 3). This process creates a hot anode vacuum arc in the first half cycle where vaporized metal expands into the cavity with a high pressure, low temperature molybdenum plasma.<sup>24</sup> During this ablation stage, an uncollimated supersonic jet is injected into the chamber through a flared nozzle that creates a  $\sim 65^\circ$  cone boundary.<sup>27</sup> The uncollimated supersonic jet boundary separates a cone of higher density and temperature plasma overlaid in a less dense background gas. The remnants of the

supersonic jet created during the anode cycle serve as the initial condition for the magnetically collimating stage to develop in the next half cycle where the center electrode becomes a cathode (after  $\sim 4.4 \mu s$  from the trigger) as seen in Figure 3. We refer to this initial conical plasma jet as the remnant anode jet. During the cathode cycle of the discharge, the current, guided by the external poloidal magnetic field when present, flows through the remnant anode jet which accelerates and develops into a collimated magnetized plasma jet. This plasma jet is that it is subject to kink instabilities which is analyzed in detail later. A different kind of evolution occurs when the center electrode is initially biased negative (Figure 3). In this case, current flows into the center electrode through a high current stream of electrons from small cathode spots. This forms a supersonic jet with a measurable barrel shock<sup>27</sup> in the second half cycle instead of a collimated jet.

The collimated molybdenum plasma jets generated in the second half cycle of the discharge with an initially positive biased center electrode evolve as magnetized plasma. To investigate the magnetized properties of the collimated jets,

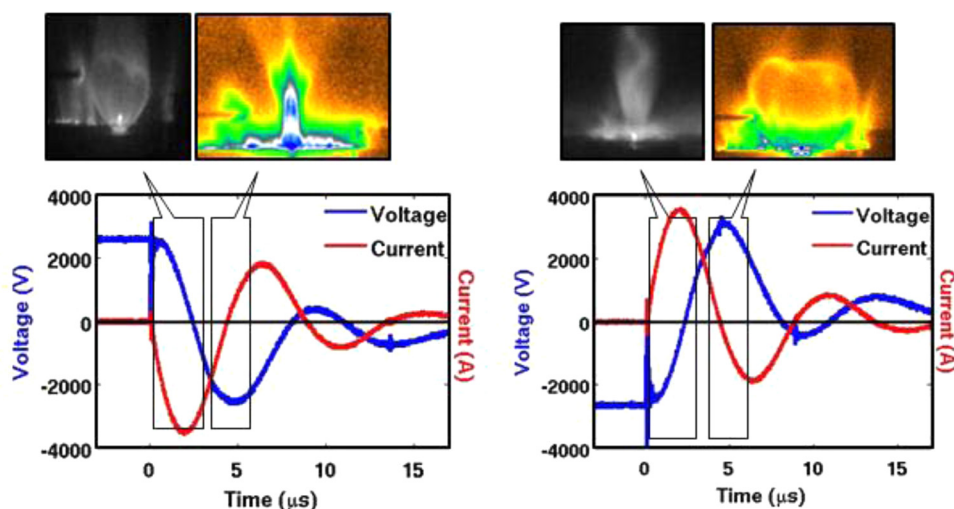


FIG. 3. (Color online) Voltage and current profiles of the capacitor discharge through the electrodes and the plasma response to both initial bias polarities. An initial positive bias produces a collimated plasma jet in the second half cycle (left), while an initial negative bias creates a supersonic jet with a measurable barrel shock (right).

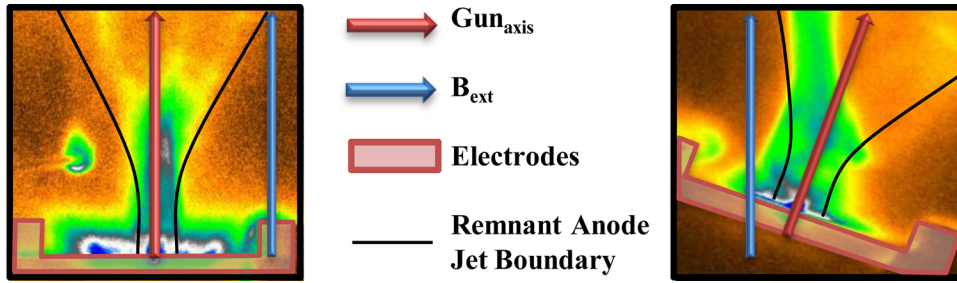


FIG. 4. (Color online) Magnetized plasma jet and remnant anode jet response when the axis of the plasma gun is aligned with respect to the external magnetic field (a) and when it is tilted with respect to the external magnetic field (b).

we tilt the axis of the plasma gun with respect to the axis of the poloidal external magnetic field as in Figure 4. The field does not affect appreciably the supersonic remnant anode jet that is ejected normal to the plasma gun in the first half cycle. This low degree of ionization plasma is mostly composed of neutrals that do not follow the field lines. The evolution of the plasma jet shows alignment with the external magnetic field for distances larger than  $\sim 2 \pm 1$  mm where we speculate  $\beta$  becomes  $< 1$ . The measured value of the uniform external magnetic field was  $B_{ext} \sim 0.45$  T with the corresponding magnetic pressure  $P_{mag} \sim 10^5$  Pa. The jet density calculated from interferograms was  $n_e = 8 \pm 4 \times 10^{22} \text{ m}^{-3}$  measured from a jet with 4900 V charging voltage at  $4.6 \mu\text{s}$  after the initial discharge and measured at the base of the jet where the density is highest. Other regions in the jet were beyond the sensitivity of the interferometer. We have no direct measurements for the plasma temperature, yet vacuum arc literature reports that the temperature under similar electrical discharge conditions is fairly constant and has a value of  $\sim 6$  eV.<sup>28</sup> We use this value qualitatively in our calculations. The plasma pressure near the center electrode is then  $P \sim 4 \times 10^5$  Pa that results in  $\beta \sim 4$ . This value is consistent with the jet being ejected close to normal to the electrode and not being affected considerably by the external magnetic field. The jet at a distance of  $\sim 2 \pm 1$  mm from the electrode has a lower density as a result of expansion ( $n \sim 10^{22} \text{ m}^{-3}$ ) leading to a pressure  $P \sim 2 \times 10^4$  Pa and consequently  $\beta \sim 0.2$ . The plasma beyond this distance is then controlled by the magnetic field as seen in Figure 4. The Reynolds number ( $R = LV / \nu_k \sim 10^3$ ) is  $\gg 1$  so that viscosity does not influence the dynamics of the jet as in astrophysical jets. The magnetic Reynolds number that represents the ratio between magnetic advection and magnetic diffusion is  $R_M = \mu_0 LV \sigma \sim 10$  (where  $L = 0.01$  m and  $V = 4 \times 10^4$  m/s are the characteristic length and velocity respectively and  $\sigma = 1.9 \times 10^4 \Omega/\text{m}$  ( $T_e = 6$  eV) is the plasma conductivity). This value suggests that electrons and magnetic field lines will evolve mostly together, similar to what is expected in astrophysical jets. The ions with a Larmor radius similar to the plasma size seem to be electrostatically confined by the electrons so that the dynamics of the plasma jet are magnetized as shown in Figure 4.

The strength of the external magnetic field determines the acceleration in the ejected jet and the subsequent maximum length for which they remain collimated before becoming unstable. The molybdenum plasma evolution with different external magnetic fields is shown in Figure 5 and in Figure 6 (enhanced). With no external magnetic field, the

boundary of the remnant anode jet, ejected in the first half cycle of the capacitor discharge, does not progress in time axially and remains anchored to the electrodes. The ejected plasma jet in the second half cycle becomes unstable near the center electrode without collimation. As the field strength is increased, the remnant anode jet cone detaches from the electrodes and progresses axially together with the magnetized plasma jet ejected in the second half cycle. The stronger the external magnetic field, the higher is the speed achieved by the magnetized plasma jet. The collimation of the jets become evident and the length for which the jets remain collimated increases with increasing magnetic fields before instabilities develop.

The kinks developed in the plasma jet column have been analyzed and compared with Kruskal-Shafranov theory of current-driven instabilities.<sup>29</sup> This condition is found in screw pinches or stabilized z-pinches where an axial plasma discharge is embedded in a background axial magnetic

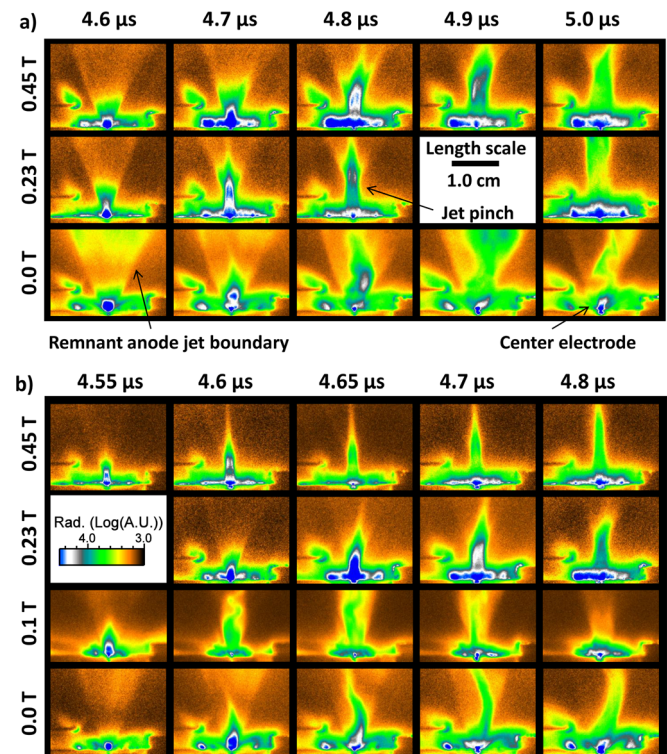


FIG. 5. (Color online) Jet evolution for different magnetic field strength and the capacitor initially charged to 4000 V in (a) and 3000 V in (b). The cathode (or second) half cycle starts at  $\sim 4.5 \mu\text{s}$  ( $I = 0$ ). Representative examples of the remnant anode jet, jet pinch, and center electrode are labeled in the figure. The color scale is logarithmic.

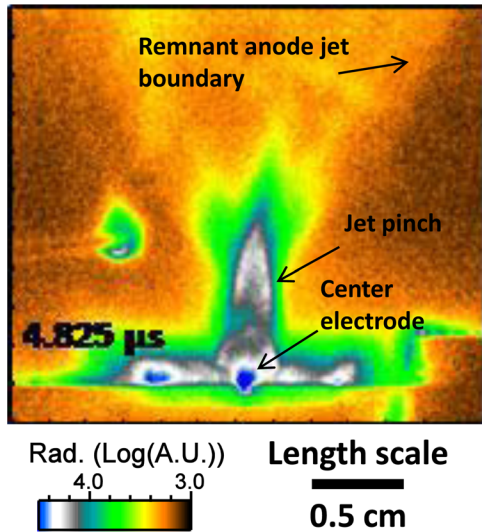


FIG. 6. (Color online) ICCD images of plasma jet evolution presented in movie form with magnetic field = 0.45 T and electrode charged to 4900 V. The half cycle starts at  $\sim 4.5 \mu\text{s}$  ( $I=0$ ). The color scale is logarithmic, independently normalized per frame basis with the color legend. The remnant anode jet, jet pinch, and center electrode are labeled in the static figure (enhanced online) [URL: <http://dx.doi.org/10.1063/1.3671953.1>].

field.<sup>30</sup> The axial current,  $I$ , generates a toroidal magnetic field,  $B_\phi$ , that is destabilizing. A perturbation in the form of a kink amplifies the toroidal field and the magnetic pressure in the concave sides of the kink while diminishing the pressure in the convex sides of the kink. The modified magnetic field amplifies the perturbation. A background axial magnetic field  $B_z$  adds magnetic pressure in the form of magnetic tension of the field lines. The more the magnetic field lines are bent, the greater the magnetic tension is which provides a stabilizing effect to the kink perturbation. The overall stability of the discharge depends on the net strength of these two opposing effects. The instability parameter  $q_{edge}$  and condition for instability is given by Eq. (1),

$$q_{edge} = 2\pi \frac{aB_z}{lB_\theta} = \frac{(2\pi a)^2 B_z}{l\mu_0 I} < 1, \quad (1)$$

where  $a$  and  $l$  are the jet radius and length, respectively.<sup>15,29</sup> For a current carrying plasma jet embedded in an external magnetic field, as the length increases the parameter  $q_{edge}$  decreases and the kink instability is more likely to occur. Figure 7 shows images of the evolution of a jet as well as the calculated  $q_{edge}$  using the measured current, external field, and dimensions from the images of the plasma emission. The measured parameters we use for the calculation in Figure 7 are the length of the visible collimated part of the jet, which varies from  $1 \pm 1$  mm to  $19 \pm 1$  mm, the radius of the visible collimated jet is  $2 \pm 0.5$  mm, the external magnetic field, measured with a Hall probe at the electrode, is  $0.4 \pm 0.1$  T. The current, measured with a Rogowski coil, ranges from  $0.3 \pm 0.2$  to  $2.7 \pm 0.1$  kA during the jet evolution in this measurement similar to the discharges in Figure 3. At early times in the discharge,  $q_{edge}$  has a value greater than 10 and the associated jet is stable. As the jet progresses in time, its length increases and  $q_{edge}$  decreases. At  $t \sim 5.1 \mu\text{s}$ ,  $q_{edge}$  approaches one and the jet develops kinks. For later times, the kink instability can be seen creating bulges and clumps. This mechanism could be the explanation for similar knots and clumps observed in several astrophysical jets.<sup>3</sup>

The knowledge of the current distribution is important in understanding the MHD forces present in the plasma and the evolution of the jets. The images suggest a flared current profile emanating from the collimated jet into the remnant anode jet closing in the outer electrode through the ambient gas. If the plasma surrounding the electrodes was very collisional, the discharge would occur across the gap between the anode and cathode as if the external magnetic field was not present. Self-generated magnetic field would create a discharge similar to that of a plasma gun. On the other hand, if collisions were low, we would expect the plasma to extend far away from the electrode and diffusion across the

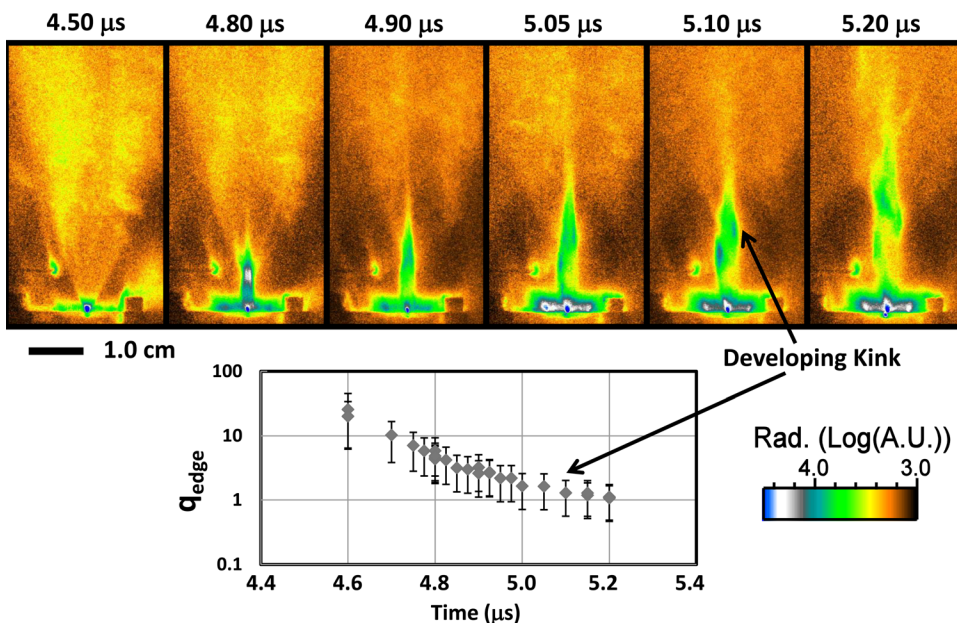


FIG. 7. (Color online) Jet evolution for an external magnetic field strength of 0.45 T and the capacitor initially charged to 4900 V. The half cycle starts at  $\sim 4.5 \mu\text{s}$  ( $I=0$ ). The color scale is logarithmic. The graph contains the calculated kink parameter  $q_{edge}$  as the jet progresses in time for the jets in this figure. The jets begin to kink after  $\sim 5 \mu\text{s}$  as observed in the images, when  $q_{edge}$  approaches 1.

magnetic field would create a uniform plasma column. The images show a regime in between these two limiting cases. While the external magnetic field and the total current were measured, direct measurements of the current and magnetic field distribution within the plasma were not made because of the small scale nature of the discharge plasma jet. Hence, we present a qualitative calculation to give evidence that the current distribution had a flared profile. We looked at the role of anisotropic conductivities in the magnetized molybdenum plasma and we used an electrostatic model to calculate an approximate current distribution using these anisotropic conductivities. A flared distribution can be obtained when the ratio between perpendicular and parallel conductivities is near unity in the jet and remnant anode region, and if the ratio is significantly smaller than unity outside the jet boundary. The exact values are not critical. The Pedersen conductivity  $\sigma_{\perp}$  in a plasma across a magnetic field and along the perpendicular electric field is

$$\sigma_{\perp} = \frac{\sigma_{\parallel}/1.96}{1 + (\Omega_e/\nu)^2}, \quad (2)$$

where  $\sigma_{\parallel} = 1.96n_e^2/(\mu m_e)$  is the parallel conductivity,  $\Omega_e$  is the electron cyclotron frequency, and  $\nu$  is the collisional frequency.<sup>31</sup> There are three distinct regions in the jets as seen in Figure 2: (1) the collimated jet, (2) the remnant anode jet, and (3) the background plasma. Using order of magnitude estimates with the parameters discussed in this paper, we chose  $n_e = 10^{22} \text{ m}^{-3}$  and  $T_e = 6 \text{ eV}$  for the collimated jet, then allowing geometrical expansion of the plasma to the remnant anode jet we would expect an order of magnitude reduction in density ( $n_e = 10^{21} \text{ m}^{-3}$ ) and a reduction in temperature ( $T_e = 1 \text{ eV}$ ). For the background plasma, we use a density slightly above the background pressure measured with a pressure gauge ( $n_e = 10^{20} \text{ m}^{-3}$ ) and another reduction in temperature ( $T_e = 0.5 \text{ eV}$ ). Low temperatures suggest  $Z \sim 1$  in these regimes. Thus, we find that  $\sigma_{\perp}/\sigma_{\parallel} \sim 0.6, 0.8,$  and  $0.3$  for regions 1 through 3, respectively, using these estimated densities and temperatures. Using these parameters, the current will flow from the grounded plate following the magnetic poloidal field lines until it reaches the flared remnant anode jet cone because the conductivity ratio is low and then the current will flow down diagonal (or the shortest spatial path) along the remnant anode jet into the magnetized plasma jet because the conductivity ratio is close to unity. The plasma velocity is mainly in the direction of the magnetic field so that the electric fields in the ion and laboratory frame of reference are similar. The electron thermal contribution to the current is small ( $\sim T_e/\text{jet radius} \sim 1 \text{ kV/m}$ ) compared to the external electric field ( $\sim 100 \text{ kV/m}$ ). The current distribution is then approximately the solution of the electrostatic problem with parallel and perpendicular conductivities with defined voltage at the boundaries. We calculated the current distribution using Maxwell SV (2D electrostatic model)<sup>32</sup> approximating the external magnetic field as uniform neglecting the self-generated magnetic field and assuming constant conductivity ratios for the regions previously mentioned. We found that the axial current in the remnant anode jet was a flared flux tube as shown in Figure 8.

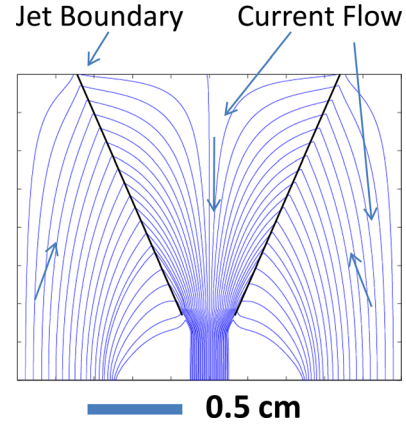


FIG. 8. (Color online) Current field lines for anisotropic conductivities of the plasma in an external magnetic field. The current distribution was calculated using an electrostatic model (Maxwell SV) approximating the external magnetic field as uniform, neglecting the self generated magnetic field, and assuming constant conductivity ratios for the various regions in the plasma with assumed and measured plasma values. The current field lines form a flared current flux tube that accelerates the plasma flow axially.

The molybdenum plasma emission distribution in the ICCD images is similar to the simulated mass distribution within a magnetic-current flux tube (Figure 9) given by the radial pressure balance derived by Bellan.<sup>33</sup> The radial pressure gradient is balanced by the magnetic force arising from the axial current profile and its toroidal magnetic field similar to a z-pinch. If we take a current profile  $I(r, z) = (r/a(z))^2 I_0$  (where  $r, z$  are the radial and axial coordinates and  $a$  is the jet

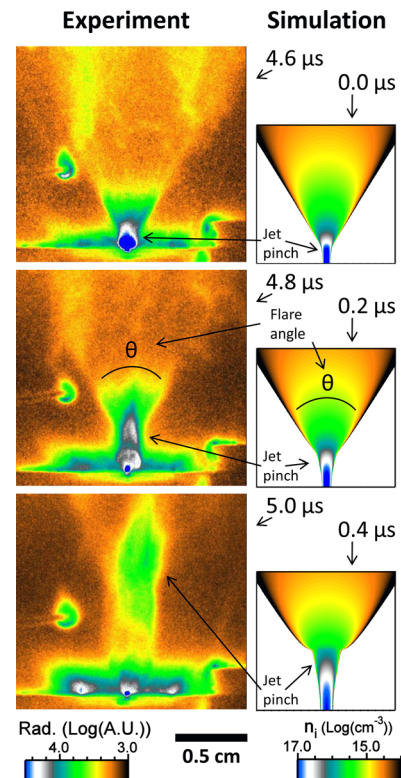


FIG. 9. (Color online) Simulated jet plasma density evolution from Eqs. (3) and (4) compared to plasma emission images taken by the ICCD. The jet pinch is the intercept of the remnant anode jet and the flare angle is the angle of the remnant anode jet.

radial boundary) the radial pressure balance yields a density given by

$$n(r, z) = \frac{1}{kT} \frac{\mu_0 I_0^2}{4\pi^2 a(z)^2} \left( 1 - \frac{r^2}{a(z)^2} \right). \quad (3)$$

The flared current profile calculated for our jets using Maxwell SV is similar to the theoretical assumption used by Bellan.<sup>33</sup> We simulated the density distribution using the measured current  $I_0 = 790 \pm 30$  A, estimated  $T_e = 6$  eV and jet radius  $a(z)$  taken from the images. The measured density of the jet near the center electrode was  $n_e = 8 \pm 4 \times 10^{22} \text{ m}^{-3}$  with 4900 V charging voltage at 4.6  $\mu\text{s}$  and agrees with the calculated density from the radial pressure balance equation  $n_e = 5 \pm 3 \times 10^{22} \text{ m}^{-3}$ . In Bellan's theory, the plasma is assumed ideal and the magnetic field flux tubes coincide with the current flux tubes. In our experiment, the flared current field lines deviate from the axial magnetic field lines. When the current flux tubes are flared, there is a net axial force arising from the pressure and magnetic forces that lead to the jet acceleration. The axial component of the force derived by Bellan<sup>33</sup> under the assumption  $I(r, z) = (r/a(z))^2 I_0$  is given by

$$F_z(r, z) = (J \times B)_z - \frac{\partial p}{\partial z} = \frac{\mu_0 I_0^2}{2\pi^2 a(z)^3} \left( 1 - \frac{r^2}{a(z)^2} \right) \frac{\partial a}{\partial z}, \quad (4)$$

which peaks on axis for a fixed position  $z_0$ .

The molybdenum jet evolution was quantified by measuring bounding lines of the conical remnant anode jet with respect to the plasma gun. The intersection of the two bounding lines of the remnant anode jet is referred here as the jet pinch (Figure 9) and its axial velocity is called the jet pinch velocity. The axial progression and the flare angle of the remnant anode jet bounding lines are shown in Figure 10. When there is no external magnetic field, the jet pinch remains in the original position and the flare angle remains constant. As the external magnetic field is increased, the jet progression occurs at higher velocities and the flare angle increases. We simulated these results qualitatively as shown in Figure 9 by solving Eqs. (3) and (4) along with the one-dimensional mass, momentum, and energy Eqs. (5)–(7), respectively, on axis with  $p = nkT$ .

$$\frac{\partial \rho}{\partial t} + v_z \frac{\partial \rho}{\partial z} + \rho \frac{\partial v_z}{\partial z} = 0, \quad (5)$$

$$\rho \left( \frac{\partial v_z}{\partial t} + v_z \frac{\partial v_z}{\partial z} \right) - F_z = 0, \quad (6)$$

$$\frac{\partial p}{\partial t} + v_z \frac{\partial p}{\partial z} + \frac{5}{3} p \frac{\partial v_z}{\partial z} = 0. \quad (7)$$

The initial conditions for the simulations shown in Figures 9 and 10 are order of magnitude estimations of the current and temperature ( $I_0 = 1000$  A and  $T_0 = 10$  eV), and the jet profile  $a_0(z)$  was estimated from the jet images ( $r = 0.5$  mm for the collimated part of  $a(z)$  and the slope of the flared part of  $a(z)$  was 0.62). The initial velocity,  $v_{z,0}$ , was estimated from the thermal expansion of the cathode jet material (assumed to be  $1.8 \times 10^4$  m/s as reported in vacuum arc literature for cathode jets under similar voltage and current conditions).<sup>28</sup> We used the initial conditions in Eqs. (3) and (4) to solve for the initial force, mass density, and pressure ( $F_{z,0}(z)$ ,  $\rho_0(z)$ , and  $p_0(z)$ , respectively, where  $z$  is along the axis of the jet) with  $r = 0$ . Equations (5)–(7) were then integrated using a 4th order Runge-Kutta integration method over a time interval of  $3.0 \times 10^{-11}$  s to solve for  $\rho_1$ ,  $p_1$ , and  $v_{z,1}$  on the jet axis. We calculated the evolved jet profile,  $a_1(z)$ , from Eq. (3) while setting  $r = 0$ , and the process was repeated to find the time evolution of these quantities. The current was kept constant since it did not change appreciably during the jet evolution. The simulated jet pinch velocity was  $v = 2.6 \times 10^4$  m/s and the measured axial jet pinch velocity under the corresponding conditions was  $v = 4.4 \pm 0.9 \times 10^4$  m/s. The difference between the simulated and measured values resides in the simplifications used to model the system. The higher acceleration that occurs near the axis increases the flare angle as shown in Figure 10.

A feature observed in the jets is a  $\sim 2$  mm long intensity depression in the emission profile on axis (Figure 11). To investigate the nature of this depression, we note that plasma emission from bremsstrahlung radiation is strongly dependent on density ( $n^2$ ) and weakly dependent on temperature.<sup>34</sup> A depression on the order of 20% in the radiated intensity on the line integrated ICCD measurements of the jets would require a local intensity drop of about one order of magnitude and a correspondingly density drop of two orders of magnitude due to the necessity of integrating the intensity through the plasma column. Using particle conservation and assuming a much smaller particle velocity upstream near the center electrode ( $\sim 10^5$  m/s) compared to downstream, it would take  $\sim 100$  ns

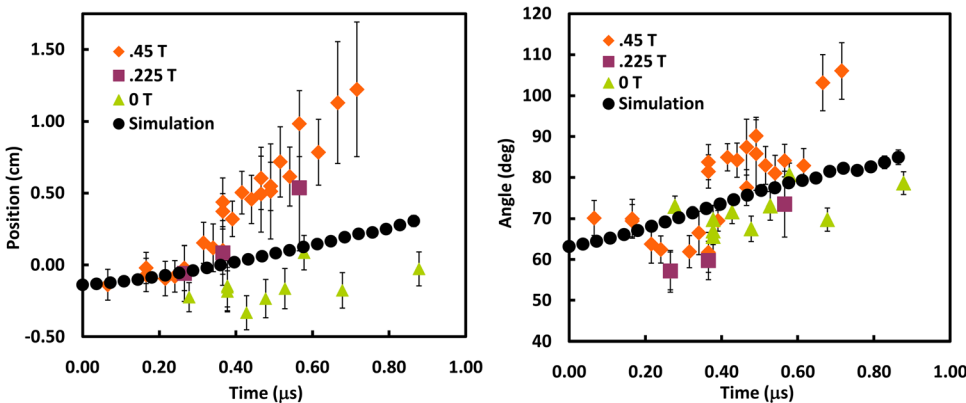


FIG. 10. (Color online) Position of the jet pinch (left) and flare angle (right) measured for different magnetic field strengths and for the simulation, as illustrated in Figure 9.

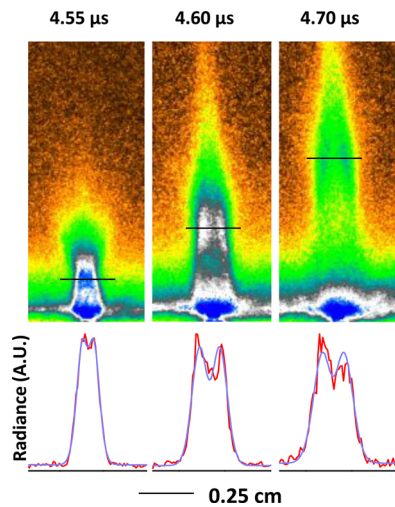


FIG. 11. (Color online) A region of lower plasma emission in the ICCD image, which we call a reduced intensity depression, evolves with the jet as shown near the horizontal black lines. The corresponding intensity line-outs at these locations are shown.

for the intensity depression to form that is similar to the time measured from the images. One could argue that this feature could be the result of higher acceleration near the axis where the axial force is the greatest, forcing plasma along the axis of the jet beyond the location of the depression, which can be seen in Figure 5. However, diffusion should quickly cancel this density drop. Another possible cause of the intensity depression is rotation in the plasma column. In Bellan's model,<sup>33</sup> significant plasma rotation can occur in fluxtubes when the current is strongly increasing, which is the state we observe in collimated jets. Significant rotation could then increase the outer density of the jet to form the observed intensity depression from centrifugal forces. Rotation has been observed in astrophysical jets<sup>35</sup> making the study of rotation in laboratory jets of interest to astrophysical research. This depression and its origin are still under investigation.

#### IV. CONCLUSION

In conclusion, we have created magnetized collimated plasma jets to study jet acceleration and collimation mechanisms. Under certain conditions, magnetized collimated plasma jets develop from supersonic unmagnetized flows by magnetohydrodynamic forces. The magnitude of an external poloidal magnetic field determines the acceleration and the final length for which the jets remain collimated. With low or no external magnetic fields, the jets become unstable at the origin while stronger magnetic fields increase the collimation length until the kink instabilities develop. These instabilities in the form of kinks have been related to current-driven instabilities and the threshold agrees well with Kruskal-Shafranov theory. The density profile evolution has been studied and the results support the MHD theory of current carrying magnetic flux tubes derived by Bellan to explain jets acceleration and collimation. The experiment has boundary conditions similar to astrophysical jets and the plasma parameters make scaling possible however magnetic diffusion and energy transport by thermal conduction is expected, rendering the scaling more qualitative. Higher den-

sity and temperature jets would create more favorable conditions with less dissipation and better scalability. The results support the importance of magnetic fields as a mechanism for astrophysical jet formation and collimation. Features created by the instabilities could explain knots and clumps observed in astrophysical jets. Finally, the plasma dimensions and parameters are different as compared to the parameters of other experiments while similarities in the jets evolution have been observed, supporting the MHD scaling theory and universality of these entities.

<sup>1</sup>T. Tajima and K. Shibata, *Plasma Astrophysics* (Addison-Wesley, Reading, Mass., 1997).

<sup>2</sup>D. L. Meier, S. Koide, and Y. Uchida, *Science* **291**, 84 (2001).

<sup>3</sup>B. Reipurth and J. Bally, *Annu. Rev. Astron. Astrophys.* **39**, 403 (2001).

<sup>4</sup>E. M. G. D. Pino, *Adv. Space Res.* **35**, 908 (2005).

<sup>5</sup>B. A. Remington, R. P. Drake, and D. D. Ryutov, *Rev. Mod. Phys.* **78**, 755 (2006).

<sup>6</sup>R. D. Blandford and D. G. Payne, *Mon. Not. R. Astron. Soc.* **199**, 883 (1982).

<sup>7</sup>W. Junor, J. A. Biretta, and M. Livio, *Nature* **401**, 891 (1999).

<sup>8</sup>P. Bellan, M. Livio, Y. Kato, S. V. Lebedev, T. P. Ray, A. Ferrari, P. Hartigan, A. Frank, J. M. Foster, and P. Nicolai, *Phys. Plasmas* **16**, 041005 (2009).

<sup>9</sup>D. D. Ryutov, R. P. Drake, and B. A. Remington, *Astrophys. J., Suppl. Ser.* **127**, 465 (2000).

<sup>10</sup>Farley, K. G. Estabrook, S. G. Glendinning, S. H. Glenzer, B. A. Remington, K. Shigemori, J. M. Stone, R. J. Wallace, G. B. Zimmerman, and J. A. Harte, *Phys. Rev. Lett.* **83**, 1982 (1999).

<sup>11</sup>Lebedev, J. P. Chittenden, F. N. Beg, S. N. Bland, A. Ciardi, D. Ampleford, S. Hughes, M. G. Haines, A. Frank, E. G. Blackman, and T. Gardiner, *ApJ*, **564**, 113 (2002).

<sup>12</sup>S. V. Lebedev, A. Ciardi, D. J. Ampleford, S. N. Bland, S. C. Bott, J. P. Chittenden, G. N. Hall, J. Rapley, C. A. Jennings, A. Frank, E. G. Blackman, and T. Lery, *Mon. Not. R. Astron. Soc.* **361**, 97 (2005).

<sup>13</sup>F. Suzuki-Vidal, S. V. Lebedev, S. N. Bland, G. N. Hall, G. Swadling, A. J. Harvey-Thompson, J. P. Chittenden, A. Marocchino, A. Ciardi, A. Frank, E. G. Blackman, and S. C. Bott, *Phys. Plasmas* **17**, 112708 (2010).

<sup>14</sup>S. C. Hsu and P. M. Bellan, *Br. Assoc. Am. Soc.* **34**, 760 (2002).

<sup>15</sup>S. C. Hsu and P. M. Bellan, *Mon. Not. R. Astron. Soc.* **334**, 257 (2002).

<sup>16</sup>S. C. Hsu and P. M. Bellan, *Phys. Rev. Lett.* **90**, 215002 (2003).

<sup>17</sup>S. C. Hsu and P. M. Bellan, *Phys. Plasmas* **12**, 2103 (2005).

<sup>18</sup>S. You, G. S. Yun, and P. M. Bellan, *Phys. Rev. Lett.* **95**, 045002 (2005).

<sup>19</sup>F. Suzuki-Vidal, S. V. Lebedev, S. N. Bland, G. N. Hall, G. Swadling, A. J. Harvey-Thompson, J. P. Chittenden, A. Marocchino, A. Ciardi, A. Frank, E. G. Blackman, and S. C. Bott, *Phys. Plasmas* **17**, 112708 (2010).

<sup>20</sup>W. Junor, J. A. Biretta, and M. Livio, *Nature* **401**, 891 (1999).

<sup>21</sup>G. V. Ustyugova, A. V. Koldoba, M. M. Romanova, V. M. Chechetkin, and R. V. E. Lovelace, *Astrophys. J.* **516**, 221 (1999).

<sup>22</sup>F. Bacciotti and J. Eisloffel, *Astron. Astrophys.* **342**, 717 (1999).

<sup>23</sup>C. Carrasco-González, L. F. Rodríguez, G. Anglada, J. Martí, J. M. Torrelles, and M. Osorio, *Science* **330**, 1209 (2010).

<sup>24</sup>R. L. Boxman, P. J. Martin, and D. M. Sanders, *Handbook of Vacuum Arc Science and Technology Fundamentals and Applications* (Noyes Publications, Park Ridge, New Jersey, USA, 1995).

<sup>25</sup>R. Benattar, C. Popovics, and R. Sigel, *Rev. Sci. Instrum.* **50**, 1583 (1979).

<sup>26</sup>J. M. Lafferty, *Vacuum Arcs Theory and Application*, 1st ed. (Wiley, New York, 1980).

<sup>27</sup>G. Scoles, D. Bassi, U. Buck, and D. Laine, *Atomic and Molecular Beam Methods* (Oxford University Press, New York, 1988), Vol. 1.

<sup>28</sup>G. A. Mesyats, *Cathode Phenomena in a vacuum Discharge: The Breakdown, the Spark and the Arc* (Nauka Publishers, Moscow, Russia, 2000).

<sup>29</sup>G. Bateman, *MHD Instabilities* (MIT, Cambridge, MA, 1978).

<sup>30</sup>J. P. Freidberg, *Ideal Magnetohydrodynamics* (Plenum Press, New York, 1987).

<sup>31</sup>S. I. Braginskii, *Rev. Plasma Phys.* **1**, 205 (1965).

<sup>32</sup>See <http://www.ansoft.com> for Ansoft Corporation, Maxwell 2D Student Version (Maxwell SV).

<sup>33</sup>P. Bellan, *Phys. Plasmas* **10**, 1999 (2003).

<sup>34</sup>I. A. B. Zeldovich and I. U. P. Raizer, *Physics of Shock Waves and High-Temperature Hydrodynamic Phenomena* (Academic Press, New York, 1966).

<sup>35</sup>F. Bacciotti, T. P. Ray, R. Mundt, J. Eisloel, and J. Solf, *Astrophys. J.* **576**, 222 (2002).